Supporting Information

High-pressure synthesis and excellent thermoelectric performance of Ni/BiTeSe magnetic nanocomposites

Shifang Ma,[a] Cuncheng Li,[a] Ping Wei,[ab] Wanting Zhu,[a] Xiaolei Nie,[a] Xiahan Sang,[ab] Qingjie Zhang[a] and Wenyu Zhao*[a]
[a]*State Key Laboratory of Advanced Technology for Materials Synthesis and Processing, Wuhan University of Technology, Wuhan, 430070, China.* E-mail: wyzhao@whut.edu.cn
[b]*Nanostructure research center, Wuhan University of Technology, Wuhan, 430070, China*

1. Effects of sintering temperature and pressure on composition

To investigate the influence of sintering temperature, these Ni/$Bi_2Te_{2.7}Se_{0.3}$ nanocomposites sintered at a low-temperature and high-pressure sintering method (300 MPa and 553-633 K) are labeled as HP553, HP573, HP593, HP613 and HP633, respectively. As shown in Fig. S1a, all the diffraction peaks of samples for sintering temperature lower than 593 K can be indexed using the crystal structure of Bi_2Te_3, indicating that the interfacial reaction between Ni-NPs and the matrix is negligible at lower sintering temperature. However, $NiTe_2$ peaks can be identified due to reaction between Ni-NPs and $Bi_2Te_{2.7}Se_{0.3}$ matrix when the sintering temperature was more than 593 K. To investigate the influence of sintering pressure, the traditionally high-temperature and low-pressure sintering (50 MPa and 633-713 K) was used to sinter the as-prepared nanocomposite powders and the samples are named as LP633, LP653, LP673, LP693 and LP713, respectively. The characteristic diffraction peaks of $NiTe_2$ can be found in all samples (Fig. S1b), indicating that Ni-NPs are unstable and can easily react with the $Bi_2Te_{2.7}Se_{0.3}$ matrix during traditionally high-temperature and low-pressure sintering process, as reported by previous literatures.[1, 2] The two sintering methods indicate that the low-temperature sintering method is preferred to suppress reaction of Ni-NPs with $Bi_2Te_{2.7}Se_{0.3}$ alloys under high pressure condition and preserve Ni-NPs.

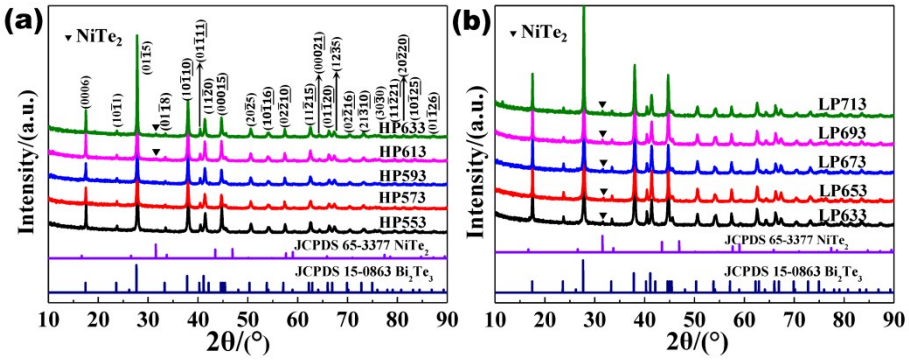

Fig. S1 XRD patterns of sintered 0.3%Ni/$Bi_2Te_{2.7}Se_{0.3}$. (a) High-pressure samples sintered in the range of 553-633 K at 300 MPa. (b) Low-pressure samples sintered in the range of 633-713 K at 50 MPa.

2. Microstructures of 0.3%Ni/$Bi_2Te_{2.7}Se_{0.3}$ sintered at 300 MPa and different temperature

As shown in Fig. S2a, the HP573 is mainly composed of $Bi_2Te_{2.7}Se_{0.3}$ and many black contrasts are distributed along the grain boundaries. We suspect that the Ni elements exist in the black contrasts position. The elemental composition of black contrasts distributed along the grain boundaries was studied by electron probe microanalysis (EPMA) equipped with energy dispersive X-ray (EDX) and the result (Fig. S2b) reveals that regions of black contrast contain Ni elements, indicating that Ni-NPs exist at the grain boundaries of the $Bi_2Te_{2.7}Se_{0.3}$ matrix. The microstructures of fracture surfaces for 0.3%Ni/$Bi_2Te_{2.7}Se_{0.3}$ sintered at low-temperature and high-pressure sintering method (300 MPa and 553-613 K) are shown in Fig. S2c-2f. It is clear that many nanoparticles are randomly distributed at the grain boundaries of $Bi_2Te_{2.7}Se_{0.3}$. Combining the results of XRD, we ensure that for sintering temperature lower than 593 K, Ni-NPs are randomly distributed at the grain boundaries of $Bi_2Te_{2.7}Se_{0.3}$ (Fig. S2c and d). However, for sintering temperature more than or

equal to 593 K, Ni-NPs and Ni-Te alloy are randomly distributed at the grain boundaries of $Bi_2Te_{2.7}Se_{0.3}$ (Fig. S2e and f) because of the reaction of Ni-NPs with $Bi_2Te_{2.7}Se_{0.3}$ induced by relatively high sintering temperature. These results further confirm that Ni-NPs were successfully preserved and incorporated into $Bi_2Te_{2.7}Se_{0.3}$ matrix by lowering the sintering temperature under the high pressure of 300 MPa.

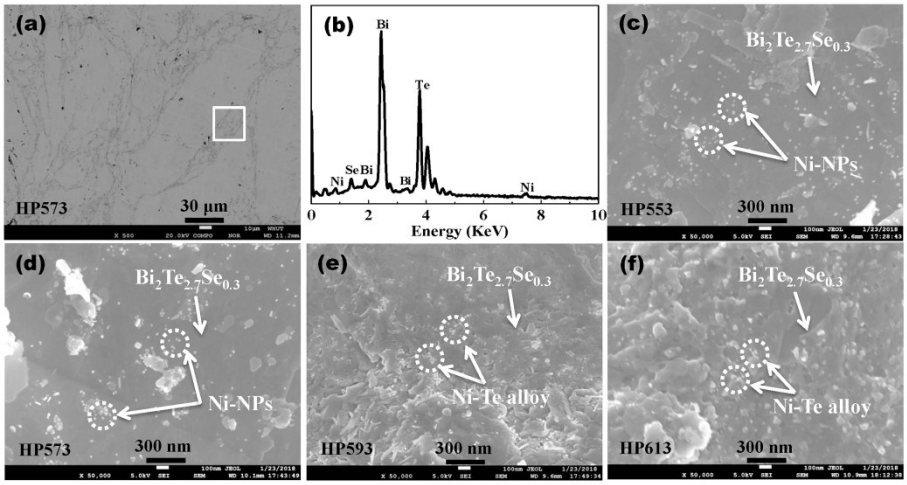

Fig. S2 Microstructures of 0.3%Ni/$Bi_2Te_{2.7}Se_{0.3}$ from EPMA and FESEM. (a) Back-scattered electron image of polished surface of HP573. (b) EDX result of the square area in (a). Secondary electron images of fracture surfaces of (c) HP553, (d) HP573, (e) HP593, and (f) HP613.

We have carefully investigated the microstructure characterization of synthesized Ni-NPs, as-prepared Ni/$Bi_2Te_{2.7}Se_{0.3}$ nanocomposite powders and SPSed Ni/$Bi_2Te_{2.7}Se_{0.3}$ nanocomposite bulk materials. Experimentally, the preparation of monodispersed Ni-NPs is not a difficult thing if enough organic dispersants are used. However, we discover that too many organic dispersants may cause the remarkable reduction in the thermoelectric and cooling performance. Therefore, we cannot use any organic dispersants in our experiment to prevent agglomeration. The synthesized Ni-NPs are 8-10 nm in size (Fig. S3a) and the crystal structure is consistent with the face-centered cubic structure (Fig. S3b). Although the agglomerations shown in Fig. S3c and e seem that the Ni-NPs in magnetic nanocomposites have grown to larger particles in SEM images, STEM images (Fig. S3f) reveals that these agglomerations consists of separated NPs with the average size the same as the as-synthesized Ni-NPs (Fig. S3a). These microstructures reveal that our preparation process may keep fine Ni-NPs in soft agglomeration state all the time. Namely, Ni-NPs embedded into $Bi_2Te_{2.7}Se_{0.3}$ matrix may be in superparamagnetic state and can generate electron multiple scattering effect.

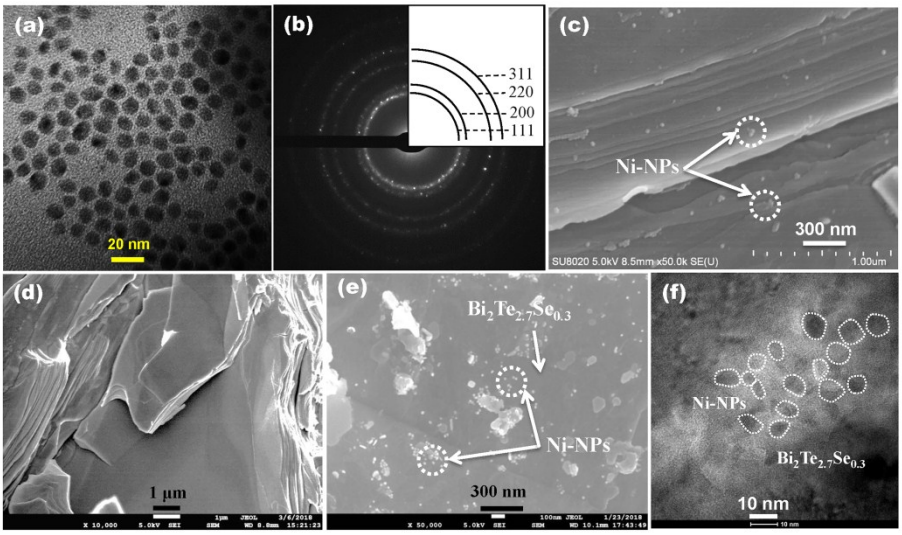

Fig. S3 (a) HRTEM image of synthesized Ni-NPs. (b) Corresponding selected area electron diffraction (SAED) pattern of (a). FESEM images of (c) nanocomposite powders (x=0.3%), (d) fracture surface of SPSed matrix, (e) fracture surface of SPSed nanocomposite material. (f) TEM image of HP573.

3. Effects of sintering temperature on density and orientation factor

The densities and XRD patterns of sintered bulk samples are displayed in Fig. S4. The relative densities and orientation factors are calculated and the results are listed in Table S1. The relative density increases with increasing sintering temperature before 613 K and keep constant as sintering temperature further increases. The diffraction peak intensity of (000*l*) and orientation factor also increases gradually with increasing sintering temperature. Therefore, we have confirmed that both density and texture increase as sintering temperature increases.

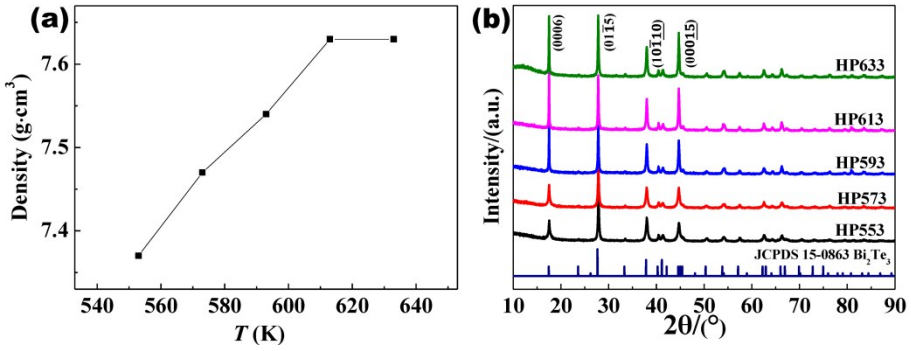

Fig. S4 (a) Densities and (b) XRD patterns of 0.3%Ni/$Bi_2Te_{2.7}Se_{0.3}$ sintered at different temperature.

Table S1. Density, relative density and orientation factor of samples sintered at different temperature.

Samples	Density (g/cm^3)	Relative density (%)	Orientation factor (000*l*)
HP553	7.37	94.82	0.21
HP573	7.47	96.17	0.26
HP593	7.54	97.11	0.26
HP613	7.63	98.15	0.34
HP633	7.63	98.15	0.33

4. Proof of charge transfer from Ni-NPS to $Bi_2Te_{2.7}Se_{0.3}$ matrix

The ultraviolet photoelectron spectroscopy (UPS) spectrum of the matrix were measured with Thermo Fisher ESCALAB 250Xi with He Iα radiation source ($h\nu$ = 21.22 eV). The Te $3d_{5/2}$ and $3d_{3/2}$ core levels were analyzed by X-ray photoelectron spectroscopy (XPS, Thermo VG Multilab 2000) with a pass energy of 25 eV and a step size of 0.05 eV. As shown in Fig. S5a, the work function of the $Bi_2Te_{2.7}Se_{0.3}$ matrix (φ_s) is determined to be about 5.46 eV according to the equation $\varphi = h\nu + E_{Cutoff} - E_F$. The work function of Ni-NPs (φ_m) with an average diameter of 8-10 nm is about 5.29-5.26 eV according to the metal sphere model.[3] The charge can transfer from Ni-NPs to the matrix at the interface because the φ_s is larger than φ_m, and the charge transfer is further confirmed by the chemical shift towards lower binding energy in XPS of Te 3*d* core levels (Fig. S5c). The band bending of the interface between metal and semiconductor and an interface potential (V_B),[4, 5] which are induced by the charge transfer (Fig. S5b), caused energy-dependent scattering of electrons (Fig. S5d). The energy-filtering effect may increase the α.

5. Infrared thermal images of DMT573 and DHP573 under different working currents

As shown in Fig. S6, the infrared thermal imaging pictures of DMT573 and DHP573 are took under different applied currents. The cooling-side temperature (T_c) firstly rises and then falls with increasing the applied current range from 0.2 A to 1.8 A, however, the heating-side temperature (T_h) continuous to increase. When the applied current is 1.0 A, the maximum temperature difference between the T_c and T_h are achieved and very close to the data that measured by thermocouples, which further prove the accuracy of measurement data from thermocouples.

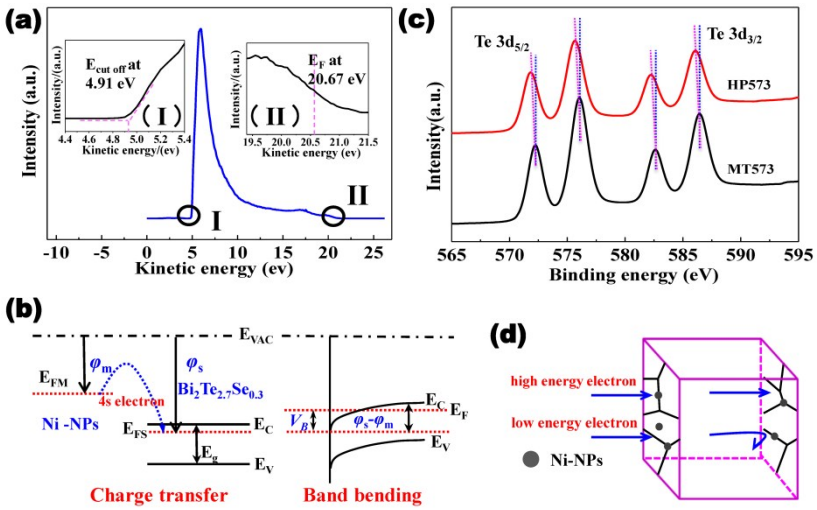

Fig. S5 Charge transfer between Ni-NPs and $Bi_2Te_{2.7}Se_{0.3}$. (a) Ultraviolet photoemission spectroscopy (UPS) spectrum of $Bi_2Te_{2.7}Se_{0.3}$ matrix. The insets are close-ups of the regions marked by black circles, highlighting the cut-off $E_{cut\text{-}off}$ (I) and Fermi edge E_F (II). (b) Schematic of the charge transfer of the 4*s* electrons from Ni-NPs to $Bi_2Te_{2.7}Se_{0.3}$ matrix and interface band bending induced by the charge transfer. (c) XPS of Te $3d_{5/2}$ and $3d_{3/2}$ core levels for MT573 and HP573. (d) Selected electron scattering induced by the interface band bending.

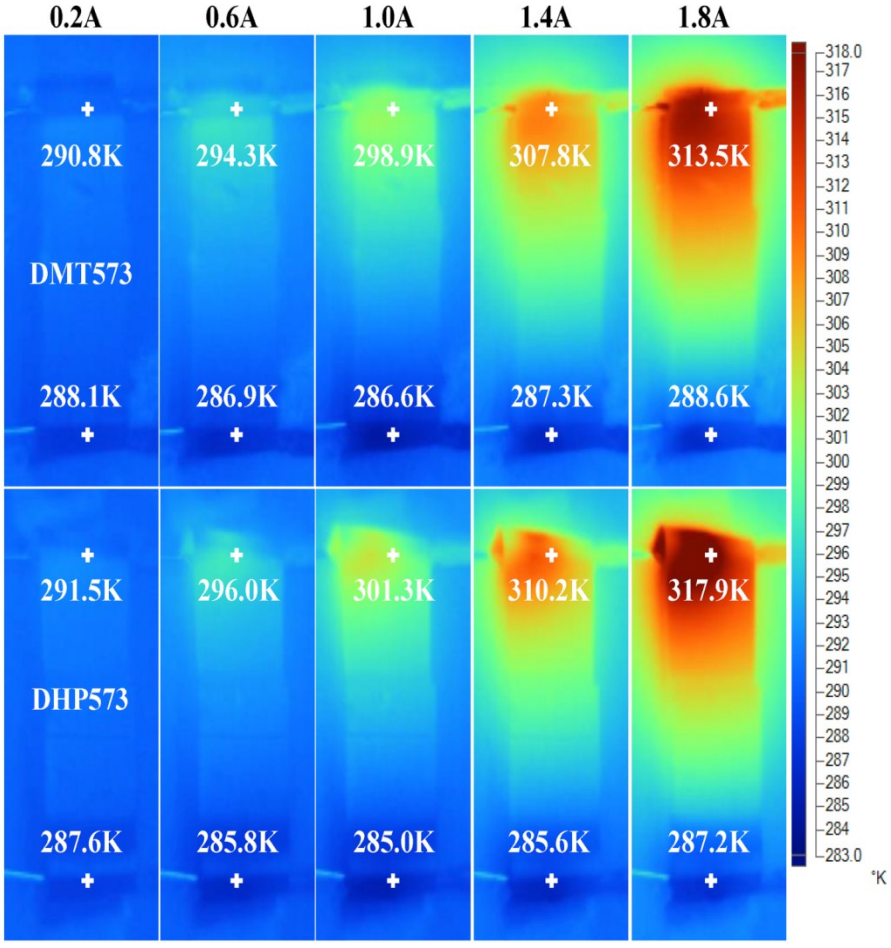

Fig. S6 Infrared thermal imaging photographs of DMT573 and DHP573.

6. Accurately Hall measurement of HP573

The traditional van der Pauw Hall measurement method enables accurate measurement of the Hall effect in semiconductor TE materials without any magnetic impurity. To avoid impact of the anomalous Hall effect induced by the magnetic nanoparticles on the Hall coefficient for the magnetic nanocomposites TE materials, a new Hall measurement method for the magnetic nanocomposites is adopted.[6] The Hall voltages ΔV_{xy} of HP573 were measured in

the range from room temperature to 500 K, when the magnetic field changes in the range of 0.1-1.2 T. The Hall voltages ΔV_{xy} in the range of 0.5-1.2 T are used to linearly fit the slope k_H. The k_H under each high-temperature condition were measured with the same method. The Hall coefficient under different temperaure can be calculated using $R_H = k_H d/(i\mu_0)$, where d is sample thickness, i is measure current, μ_0 is equal to $4\pi\times10^{-7}$ N·A^{-2}. Then, the carrier concentration (n) and Hall mobility ($_H$) were calculated according to the equations $n = 1/(R_H e)$ and $_H = \sigma/ne$, respectively (where e is electron charge). The Hall transport properties of HP573 in the range of 297-483 K are listed in Table S2.

Table S2 R_H, n, and $_H$ of HP573 under different measurement temperature.

Temperature (K)	k_H (10^{-11}V·m·A^{-1})	R_H (10^{-1}cm^3·C^{-1})	n (10^{19} cm^{-3})	μ_H (cm^2·V^{-1}·s^{-1})
297	-1.21	-1.34	4.64	131.60
333	-1.19	-1.33	4.71	113.44
363	-1.16	-1.30	4.82	100.53
393	-1.11	-1.24	5.04	88.30
423	-1.06	-1.18	5.30	78.40
453	-0.98	-1.09	5.74	68.91
483	-0.88	-0.98	6.36	60.38

7. Calculation of scattering factor of 0.3%Ni/$Bi_2Te_{2.7}Se_{0.3}$ and $Bi_2Te_{2.7}Se_{0.3}$

It is well known that the α of TE materials is inversely proportional to the n. However, the α and n of HP573 are larger than that of MT573. We suspect that the abnormal phenomenon is caused by superparamagnetic Ni-NPs. Therefore, the scattering parameter (r) of HP573 was calculated according to a single parabolic band (SPB) model and the obtained data lists in Table S3.[7, 8] The r of HP573 is larger than the MT573. Since Ni-NPs are in superparamagnetic state above room temperature, thus the magnetic moments must randomly change directions because of thermal fluctation. As a result, the multiple electron scattering is produced due to the superparamagnetic magnetic moment fluctuation of Ni-NPs. The thermal-electro-magnetic effect can hinder electron transport and effectively enhance the r.

Table S3 Charge transport properties and scattering factors of 0.3%Ni/$Bi_2Te_{2.7}Se_{0.3}$ and $Bi_2Te_{2.7}Se_{0.3}$ TE materials at room temperature.

samples	R_H (10^{-1}cm^3·C^{-1})	μ_H (cm^2·V^{-1}·s^{-1})	n (10^{19} cm^{-3})	σ (10^4 S·m^{-1})	α (μV·K^{-1})	r
MT573	-1.45	139.99	4.32	8.98	-177.36	-0.50
HP573	-1.34	129.88	4.65	9.67	-184.00	-0.36

Supplementary references

1 X. T. Dai, Y. Yu, F. Q. Zu, Z. Y. Huang. *Mater. Sci. Forum,* 2016, 847, 177-183.

2 S. M. Yoon, P. Dharmaiah, O. E. Femi, C. H. Lee, S. J. Hong. *Mater. Chem. Phys.,* 2017, 195, 49-57.

3 D. M. Wood. *Phys. Rev. Lett.,* 1981, 46, 749.

4 S. V. Faleev, F. Léonard. *Phy. Rev. B,* 2008, 77, 214304.

5 M. Zebarjadi, K. Esfarjani, A. Shakouri, J. H. Bahk, Z. Bian, G. Zeng, J. Bowers, H. Lu, J. Zide, A. Gossard. *Appl. Phys. Lett.,* 2009, 94, 202105.

6 W. Y. Zhao, Z. Y. Liu, Z. G. Sun, Q. J. Zhang, P. Wei, X. Mu, H. Y. Zhou, C. C. Li, S. F. Ma, D. Q. He, P. X. Ji, W. T. Zhu, X. L. Nie, X. L. Su, X. F. Tang, B. G. Shen, X. L. Dong, J. H. Yang, Y. Liu, J. Shi. *Nature,* 2017, 549, 247-251.

7 A. Pakdel, Q. S. Guo, V. Nicolosi, T. Mori. *J. Mater. Chem. A,* 2018, 6, 21341-21349.

8 G. Y. Xu, P. Ren, T. Lin, X. F. Wu, Y. H. Zhang, S. Niu, T. P. Bailey. *J. Appl. Phys.,* 2018, 123, 015101.